arXiv:physics/0312061v1 [physics.ins-det] 10 Dec 2003

UASLP-IF-03-007

Instrumentation

Jürgen Engelfried
Instituto de Física, Universidad Autónoma de San Luis Potosí, Mexico
jurgen@ifisica.uaslp.mx, http://www.ifisica.uaslp.mx/~jurgen/

Abstract
In this course, given at the school in 3 parts of 75 minutes each, we will discuss the physics of particle detection, the basic designs and working principles of detectors, and, as an example with more details, some detectors for particle identification.

1. Introduction

The detection and identification of particles and nuclei is not only important in high-energy physics, but also in cosmic ray and nuclear physics. The basic idea is that every effect of particles or radiation can be used as a working principle for a detector. The main purpose is the detection and identification of particles with mass m and charge z. In particle physics, the charge is usually $z = 0, \pm 1$, but in nuclear, heavy ion physics, or cosmic rays, also higher charges are possible.

Examples of effects used for particle detection and identification include the momentum p measured by deflecting a charged particle (charge z) in a magnetic field ($\rho \propto p/z = \gamma m \beta c/z$); the velocity v measured by the time of flight t ($\beta = v/c \propto 1/t$) or the Cherenkov angle ($\theta_C = 1/(\beta n)$), the total energy E measurements with a calorimeter, and for charge z measurement the ionization energy loss ($dE/dx \propto z^2$). With all the information together one can determine the quadri-vector of the particle.

The basic detection techniques work mostly for charged particles only; neutral particles are usually detected indirectly via reactions producing charged particles.

Designing instrumentation and detectors requires knowledge of the basic physics of interactions of charged and neutral particles with matter, mechanical engineering, electrical engineering (high voltage), electronic engineering, interfaces to trigger, data acquisition and computing, software engineering (calibration), and operation (stability). To know any one of them is not sufficient; all have to be applied together to build, operate and use an instrument for a physics measurement. The final goal of the measurement and the precision (resolution) needed has always to be kept in mind, in order not to over-design the instrument.

The recommended literature includes, in addition to references throughout the lecture, the following: *Particle Detectors* by Claus Grupen [1], *Detectors for particle radiation* by Konrad Kleinknecht [2], *Introduction to Experimental Particle Physics* by Richard C. Fernow [3], *Calorimetry* by Richard Wigmans [4], lecture notes and proceedings of ICFA Instrumentation Schools [5], which are held bi-yearly since 1987, recently also as regional schools, and the *Particle Data Book* [6], which contains short summaries of important topics. In the new 2004 edition [7] a rewritten and upgraded section about instrumentation will be included.

[0] Lecture course given at the 2nd Latin American School of High Energy Physics, San Miguel Regla, Mexico, June 1-14, 2003. To be published in a CERN Yellow Report.

Part I: Physics of Particle Detection

2. Interactions of Charged Particles

2.1 Kinematics

To introduce variables used throughout this lecture, let us review some basic kinematic formulas:

The maximum kinetic energy an electron (mass m_e) can gain when a particle with mass m, Energy E, momentum p, and velocity $v = \beta c$ collides with it is (by conservation of momentum and energy)

$$E_{\text{kin}}^{\max} = \frac{2m_e c^2 \beta^2 \gamma^2}{1 + 2\gamma \frac{m_e}{m} + \left(\frac{m_e}{m}\right)^2} = \frac{2m_e p^2}{m^2 + m_e^2 + 2m_e E/c^2} \tag{1}$$

In the limit of low energy ($2\gamma \frac{m_e}{m} \ll 1$) and a massive particle ($m \gg m_e$), this leads to

$$E_{\text{kin}}^{\max} = 2m_e c^2 \beta^2 \gamma^2 \tag{2}$$

and in the relativistic limit ($E_{\text{kin}} \approx E$, $pc \approx E$)

$$E^{\max} = \frac{E^2}{E + m^2 c^2 / 2m_e} \tag{3}$$

In the special case of an electron-electron collision ($m = m_e$)

$$E_{\text{kin}}^{\max} = \frac{p^2}{m_e + E/c^2} = \frac{E^2 - m_e^2 c^4}{E + m_e c^2} = E - m_e c^2 \tag{4}$$

The scattering angle Θ of a particle with charge z on a nucleus with charge Z, under an impact parameter b is given by

$$\Theta = \frac{2z \cdot Z \cdot e^2}{\beta c b} \cdot \frac{1}{p} \tag{5}$$

and leads to the Rutherford cross section σ, given by

$$\frac{d\sigma}{d\Omega} = \frac{z^2 Z^2 r_e^2}{4} \left(\frac{m_e c}{\beta p}\right)^2 \frac{1}{\sin^4 \Theta/2} \tag{6}$$

For multiple scattering by a particle passing matter of Radiation Length X_0 (see equation 29) the root mean square angle (the average angle is 0) in a plane is given by

$$\sqrt{\langle \Theta^2 \rangle} = \Theta_{\text{plane}} = \frac{13.6\,\text{MeV}}{\beta c p} z \cdot \sqrt{\frac{x}{X_0}} \left\{1 + 0.038 \ln\left(\frac{x}{X_0}\right)\right\} \tag{7}$$

and in space by

$$\Theta_{\text{space}} = \sqrt{2}\,\Theta_{\text{plane}} \tag{8}$$

Usually this distribution is approximated by a Gaussian

$$P(\Theta)\,d\Theta = \frac{1}{\sqrt{2\pi}\Theta_{\text{plane}}} \exp\left\{-\frac{\Theta^2}{2\Theta_{\text{plane}}^2}\right\} d\Theta \tag{9}$$

which describes well low angle behavior but underestimates the frequency of large angle scatters.

2.2 Energy Loss of Charged Particles

The interaction of charges particles with matter is dominated by the electromagnetic interaction, via the exchange of virtual or real photons. Virtual photons are absorbed by the atoms of the material which leads to ionization and/or excitation of the atoms. Real photons, also called radiation, is emitted by a charged particle if: 1. its velocity is faster than the velocity of light in the medium ($v > c/n$) and is called *Cherenkov radiation.* 2. if the vector velocity relative to the phase velocity of photons in matter ($\vec{v}/c_{\rm ph} = \vec{v} \cdot n/c$) changes, which has different names. A change of $|\vec{v}|$ is called *Bremsstrahlung*, a change in the direction of $\vec{v}$ *Synchrotron radiation* and a change in n *Transition Radiation.*

2.2.1 Mean Ionization Energy Loss (Bethe-Bloch formula)

We follow here the derivation in [1]. The momentum transfer per target electron, for an impact parameter b (see also equation (5)) is given by

$$p_b = \frac{2 r_e m_e c}{b\beta} z \tag{10}$$

The Energy transfer ϵ in this collision is given in a classical approximation by

$$\epsilon = \frac{p_b^2}{2m_e} = \frac{2 r_e^2 m_e c^2}{b^2 \beta^2} z^2 \tag{11}$$

The interaction rate Φ, measured in cm^2/g, with an atomic cross section σ, is given by

$$\Phi[\mathrm{g}^{-1}\mathrm{cm}^2] = \frac{N_A}{A}\,\sigma[\mathrm{cm}^2/\mathrm{atom}] \tag{12}$$

where N_A is Avogadro's number, and A atomic mass of the material. In an annulus of area $2\pi b\,db$, and Z electrons per atom, the interaction rate is

$$\Phi(\epsilon)\,d\epsilon = \frac{N_A}{A} 2\pi b\,db\,Z \tag{13}$$

equation (11) can be re-written to

$$b^2 = \frac{2 r_e^2 m_e c^2}{\beta^2}\, z^2\, \frac{1}{\epsilon} \tag{14}$$

leading to an interaction rate as function of the energy transfer

$$\Phi(\epsilon)\,d\epsilon = \frac{N_A}{A}\,\pi\,\frac{2 r_e^2 m_e c^2}{\beta^2}\, z^2\, Z\, \frac{d\epsilon}{\epsilon^2} \tag{15}$$

The energy loss dE in a small path length dx is simply the integral over all energy transfers

$$-\frac{dE}{dx} = \frac{2\pi N_A}{A}\, Z \int_0^\infty \epsilon\, b\, db = 2\pi\, \frac{Z\, N_A}{A}\, \frac{2 r_e^2 m_e c^2}{\beta^2}\, z^2 \int_0^\infty \frac{db}{b} \tag{16}$$

We are now left with the problem that this Integral is divergent for $b \to 0$ and $b \to \infty$.

For $b \to 0$ we assume a minimum impact parameter $b_{\min}$ given by half the de Broglie wavelength of the particle; smaller structures can not be resolved. $b_{\min} = h/(2p) = h/(2\gamma m_e \beta c)$. For $b \to \infty$, we make a model that for large b, the interaction time τ_i will be larger than the revolution time τ_R of the electrons in the target atom. The atom will then appear neutral to the passing particle, and no interaction will happen. The interaction time is the Lorentz-contracted fly-by time $\tau_i = b\sqrt{1-\beta^2}/v$, and the revolution time can be parametrized by $\tau_R = 1/(v_Z \cdot Z) = h/I$, I being the mean excitation energy

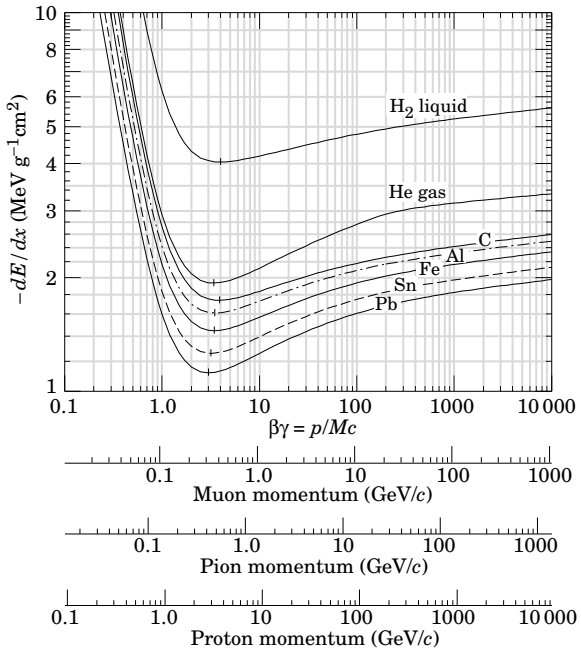

Fig. 1: Mean energy loss for different materials [6].

of the atom, where $I \approx 10\,\mathrm{eV} \cdot Z$. Requesting $\tau_i = \tau_R$ leads to $b_{\max} = \gamma h \beta c / I$. Finally, integrating equation (16), we obtain

$$-\frac{dE}{dx} = 2\pi \frac{Z\,N_A}{A} \frac{2 r_e^2 m_e c^2}{\beta^2} z^2 [\ln \frac{2\gamma^2\beta^2 m_e c^2}{I} - \eta] \tag{17}$$

The parameter η takes into account the screening effect from nearby atoms. The previous derivation assumed one single atom.

A more exact treatment, summarized in [6], gives as the final result for the Bethe-Bloch formula

$$-\frac{dE}{dx} = 2\pi \frac{Z\,N_A}{A} \frac{2\,r_e^2\,m_e\,c^2}{\beta^2} z^2 \Big[\frac{1}{2} \ln \frac{2\,m_e\,c^2\gamma^2\beta^2}{I^2}\beta^2 - \frac{\delta}{2}\Big] \tag{18}$$

The density correction takes a more complicated form, and can be described by

$$\frac{\delta}{2} = \ln \frac{\hbar\omega_p}{I} + \ln \beta\gamma - \frac{1}{2} \quad \hbar\omega_p = \sqrt{4\pi N_e r_e^2}\,\frac{m_e\,c^2}{\alpha} \tag{19}$$

where N_e is the electron density and ω_p the plasma frequency of the absorbing material, and α the Sommerfeld fine structure constant.

In fig. 1 (taken from [6]) we show examples for energy loss in different materials. The minimum energy loss of all particles in nearly all materials occurs at $3 \leq \beta\gamma \leq 4$, and is in the range of MeV/(g/cm^2) (examples: helium: $-dE/dx = 1.94\,$MeV/(g/cm^2), uranium: $1.08\,$MeV/(g/cm^2)) with the exception of hydrogen, in which particles experience a larger energy loss ($Z/A = 1$). Due to the $\ln\gamma$ term the energy loss increases for relativistic particles and reaches the so-called Fermi-Plateau due to the density effect. In gases the plateau is typically $\approx 60\,\%$ higher as the minimum.

Due to the increased energy loss at smaller $\beta\gamma$, particles will deposit most of their energy at the end of their track, just before they will be completely stopped. This "Bragg Peak" is used for the treatment of deep-seated tumors, selecting the particle type and initial energy to optimize the energy loss close to the tumor location, avoiding too much damage to tissue above the tumor.

2.2.2 Landau Distribution of the energy loss

The energy loss is distributed asymmetrically around the mean energy loss described by the Bethe-Bloch formula (eq. 18); the distribution can be approximated by the Landau distribution $\Omega(\lambda)$

$$\Omega(\lambda) = \frac{1}{\sqrt{2\pi}}\, e^{-\frac{1}{2}(\lambda + e^{-\lambda})} \tag{20}$$

where $\lambda = (\frac{dE}{dx}) - (\frac{dE}{dx})^{\mathrm{m.p.}}/(0.123\,\mathrm{keV})$, with $(\frac{dE}{dx})^{\mathrm{m.p.}}$ being the most probable energy loss. In gases and thin absorbers the Landau fluctuations have to be considered; for example a particle with $\beta\gamma = 4$ in Argon experience a most probable energy loss of $(\frac{dE}{dx})^{\mathrm{m.p.}} = 1.2\,\mathrm{keV/cm}$ and a mean energy loss of $\langle\frac{dE}{dx}\rangle = 2.69\,\mathrm{keV/cm}$.

For particle identification, one has to sample often (typically 160 times or more) to measure the Landau distribution and use adequate algorithms (e.g. "truncated mean") to obtain the mean energy loss.

Examples for successful application of this particle identification method can be found in the literature [8, 9, 10].

2.3 Scintillation

Scintillation is the de-excitation of previously exited atoms, molecules or materials. It appears in inorganic crystals, organic liquids or plastics, and gases.

In inorganic crystals, scintillation is usually an effect of the lattice. Energy lost by a passing particle is used to produce electron-hole pairs or excitons, which de-excite at activation centers (crystal imperfections) emitting photons. Common materials used include Thallium-doped NaI and CsI, BaF_2, and BGO (Bismuth-Germanium-Oxide).

Organic scintillators in liquids or plastic come in three components: the primary scintillator (antracene $C_{14}H_{10}$, naphthalene $C_{10}H_8$); a wavelength shifter (POPOP $C_{24}H_{16}N_2O_2$ 1.4-Bis-[2-(5-phenyloxazolyl)]-benzene, BBO $C_{27}H_{19}NO$ 2.5-di-(4-biphenyl)-oxazole) and a base material like mineral oil or PMMA ($C_5H_8O_2$ polymethylmetacralate).

In gases, the atoms or molecules previously excited or ionized by dE/dx emit photons due to recombination or de-excitation. This is often a background and noise source when using effects for measurements, for example Cherenkov. Basically all gases (Xe, Kr, Ar, N_2) exhibit this behavior.

The light yield (number of photons N) is a non-linear function of the energy and shows a saturation behavior, usually described by Birk's formula

$$N = N_0\, \frac{dE/dx}{1 + k_B \cdot (dE/dx)} \tag{21}$$

where $k_B \approx 0.01\,\mathrm{g/MeV\,cm^2}$ is the so-called Birk's density Parameter. Recently some better approximation were developed by a Mexican group [11].

Typically about $100\,\mathrm{eV}$ energy loss are necessary to produce one photon. The addition of wavelength shifters is necessary to avoid self-absorption of the produced photons.

2.4 Cherenkov Radiation

A charged particle with a velocity v larger than the velocity of light in a medium emits light [12]. The threshold velocity v_{thres} is given by

$$\beta_{\mathrm{thres}} = \frac{v_{\mathrm{thres}}}{c} \geq \frac{1}{n}, \quad \text{or} \quad \gamma_{\mathrm{thres}} = \frac{n}{\sqrt{n^2 - 1}} \tag{22}$$

n being the (wavelength dependent) refractive index of the material. The angle of emission is given by

$$\cos\theta_c = \frac{1}{\beta\, n} = \frac{1}{\frac{v}{c}\, n} \tag{23}$$

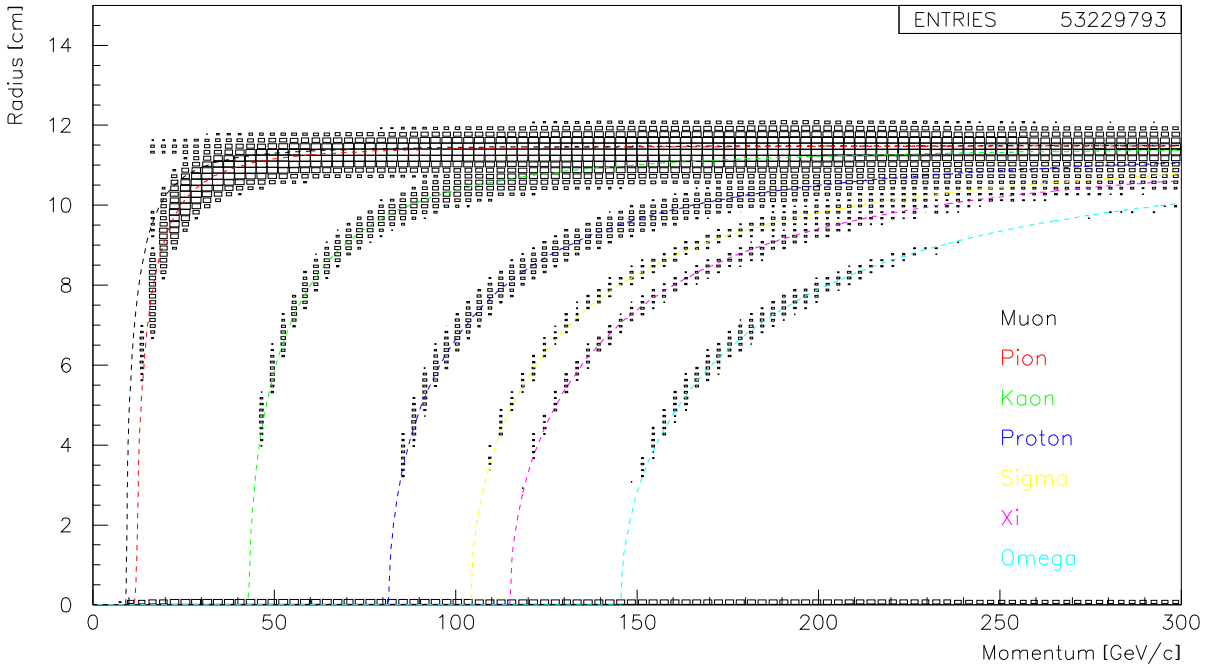

Fig. 2: Radius of imaged Cherenkov photons measured by the SELEX RICH [15] as function of the momentum for 53 million single negative track events

with a maximum angle of $\theta_c^{\max} = \arccos 1/n$. For water $\theta_c^{\max} = 42°$, for Neon at 1 atm $\theta_c^{\max} = 11$ mrad The number of photons emitted by Cherenkov radiation is [13]

$$\frac{d^2N}{dEdl} = \frac{\alpha z^2}{\hbar c}\left(1 - \frac{1}{(\beta n)^2}\right) = \frac{\alpha z^2}{\hbar c}\sin^2\theta_c \tag{24}$$

$$\frac{d^2N}{d\lambda dl} = \frac{2\pi\alpha z^2}{\lambda^2}\sin^2\theta_c \tag{25}$$

Water Cherenkov counters were originally developed to set limits on the lifetime of protons, but got converted for (solar) neutrino detection. On example is (Super-)Kamiokande. Cherenkov effect in water is also used in the tanks of the Auger Experiment to detect muons produced in cosmic ray air showers.

The simplest Cherenkov devices are threshold Cherenkov counter, only using the difference between no light or light to set ranges for the velocity of particles. A recent example is the Belle Detector [14].

Ring Imaging Cherenkov Detectors not only use the threshold information, but actually measure with the help of some imaging system (see also section 16.2) the Cherenkov angle, obtaining the velocity of the particle. A recent example for this is the SELEX RICH [15], were we show the dependency of the ring radius (or the Cherenkov angle) on the particle momenta.

2.5 Transition Radiation

Transition radiation is emitted due to the reformation of the particle field while traveling from a medium with dielectric constant ϵ_1 to a medium with ϵ_2. The energy of the radiation emitted at a single interface S is given by

$$S = \frac{\alpha\hbar z^2}{3}\frac{(\omega_1 - \omega_2)^2}{\omega_1 + \omega_2}\gamma \tag{26}$$

Material	X_0 [g/cm^2]	X_0 [cm]	$E^e_{\rm crit}$ [MeV]
air	37	30000	84
iron	13.9	1.76	22
lead	6.4	0.56	7.3

Table 1: Typical values for the Radiation length X_0

were ω_1 and ω_2 are the plasma frequencies. Typical values are for air $\omega_1 = 0.7\,\text{eV}$ and polypropylene $\omega_2 = 20\,\text{eV}$. The spectral and angular dependence of Transition Radiation is

$$\frac{d^2}{d\vartheta d\omega} = \frac{2e^2}{\pi c}\left(\frac{\vartheta}{\gamma^{-2}+\vartheta^2+\omega_1^2/\omega^2} - \frac{\vartheta}{\gamma^{-2}+\vartheta^2+\omega_2^2/\omega^2}\right)^2 \tag{27}$$

Most of the radiation is emitted in a cone with half angle $1/\gamma$, forward in the particle direction. For large photon energies $\omega > \gamma\omega_2 \approx 20-30\,\text{KeV}$, the intensity drops like $\propto \gamma^4/\omega^4$, at medium energies $\gamma\omega_1 \lesssim \omega \lesssim \gamma\omega_2$, we can observe a logarithmic decrease with ω, and at small energies $\omega < \gamma\omega_1 \approx 1\,\text{KeV}$, the intensity is almost constant. The probability to emit a KeV photon is only $\approx 10^{-2}$; to have a detectable rate, one needs to use a lot of interfaces, usually a stack of radiator foils.

A minimum foil thickness is needed for the particle field to reach an equilibrium inside the medium. The transitions into and out of the foil produce the same radiation ($(\omega_1-\omega_2)^2$ in eq. 26), so interference effects can occur, also when the foils are space equally. Part of the radiation is re-absorbed in subsequent foils ($\propto Z^5$), and low-Z materials (mylar, CH_2, carbon fibers, lithium, thickness $30\,\mu$m, distance: $300\,\mu$m are consequently used.

2.6 Bremsstrahlung

Bremsstrahlung is emitted when a charged particle experiences some acceleration. The change in energy is given by

$$-\frac{dE}{dx} = 4\alpha N_A \frac{Z^2}{A} z^2 \left(\frac{e^2}{mc^2}\right)^2 E \ln\frac{183}{Z^{1/3}} \tag{28}$$

which can be used to define via $-\frac{dE}{dx} = \frac{E}{X_0}$ the Radiation Length X_0. The PDG [6] gives a fit to estimate X_0 for different materials:

$$X_0 = \frac{716.4\,A}{Z(Z+1)\,\ln(287/\sqrt{Z})}\,[\text{g/cm}^2] \tag{29}$$

Typical values for X_0 are given in table 1. The particle energy where the ionization energy loss is equal to the energy loss by Bremsstrahlung is called the *Critical Energy* and is given for electrons by $E^e_{\rm crit} = 610\,\text{MeV}/(Z+1.24)$ for solids and liquids and $E^e_{\rm crit} = 710\,\text{MeV}/(Z+0.92)$ for gases. As seen in eq. 28, $-dE/dx \propto 1/m^2$, so Bremsstrahlung from electrons dominates; but for muons in iron $E^\mu_{\rm crit} = 960\,\text{GeV}$ so at TeV energies we have to rethink the "all penetrating μ" and can consider Muon Calorimetry. Bremsstrahlung is an important component of electromagnetic cascades (Calorimetry), which will be discussed in section 5.

2.7 Direct Electron Pair Production

In the Coulomb field of a nucleus electron pairs can be produced directly via virtual photons. The corresponding energy loss is $\propto E$ for large Energies, the same behavior as in the case of Bremsstrahlung and nuclear interactions (see sections 3.). The range of muons in rock is heavily influenced by this interaction, and yields $140\,\text{m}$ ($E_\mu = 100\,\text{GeV}$), $800\,\text{m}$ ($E_\mu = 1\,\text{TeV}$), and $2300\,\text{m}$ ($E_\mu = 10\,\text{TeV}$). For this reason experiments requiring low backgrounds have to be performed in deep (gold-)mines to be shielded from atmospheric muons produced by cosmic rays.

	Al	Fe	Pb	Air
λ_I [cm]	26.2	10.6	10.4	48000
λ_I [g/cm]	70.6	82.8	116.2	62.0

Table 2: Nuclear Interaction length λ_I for some materials.

3. Nuclear Interactions

This effect is important for the detection of neutral particles. The total cross section $\sigma_{\rm tot} \approx 50\,$mbarn can be separated in an elastic and an inelastic part; the latter is $\sigma_{\rm inel} \propto A^\alpha$, with $\alpha = 0.71$. As in the Bremsstrahlung case (eq. 29), a *Nuclear Interaction length* λ_I and a *Nuclear Absorption length* λ_a can be defined via $\lambda_I = A/(N_A\,\rho\,\sigma_{\rm tot})$ and $\lambda_a = A/(N_A\,\rho\,\sigma_{\rm inel})$. Typical values are shown in table 2. By comparing with table 1 one can conclude that for most material $\lambda_I, \lambda_a > X_0$.

The multiplicity in nuclear inelastic interactions grows logarithmically with E, and the secondary particles leave with an average transverse momentum $p_T \approx 350\,{\rm MeV}/c$.

4. Interactions of Neutral Particles

4.1 Interactions of Photons

Photons are, in contrary to charged particles, attenuated in matter; The intensity I after a distance x is given by $I = I_0\,e^{-\mu x}$, where μ is the so-called *Mass Attenuation Coefficient.* Three basic processes contribute to the $\mu = \frac{N_A}{A}\sum_{i=1}^{3}\sigma_i$: 1) The Photoelectric Effect; 2) Compton Scattering; 3) Pair Production. Each of the processes has its own energy dependence, and we will discuss them in the following sections.

4.1.1 Photoelectric Effect

One photon of sufficient energy is absorbed by an atom, releasing one electron and leaving behind a positive ion. The released electron comes predominantly from the K-shell. The effect presents a complicated energy and Z dependence,

$$\sigma^K_{\rm photo} = \left(\frac{32}{\epsilon^7}\right)^{1/2}\,\alpha^4\,Z^5\,\sigma_{\rm Thomson}\;\;[{\rm cm}^2/{\rm atom}] \tag{30}$$

with $\epsilon = E_\gamma/m_e c^2$ and $\sigma_{\rm Thomson} = (8/3)\pi\,r_e^2 = 665\,$mbarn.

4.1.2 Compton Scattering

The Compton effect describes the elastic scattering of photon on a (quasi-)free electron, a text book example to prove that the photon can be treated as a particle. At high energies, the Compton cross section $\sigma_C \propto \frac{\ln\epsilon}{\epsilon}\cdot Z$ and the energy of the photon after scattering E'_γ is related to the scattering angle θ via

$$\frac{E'_\gamma}{E_\gamma} = \frac{1}{1+\epsilon(1-\cos\theta_\gamma)} \tag{31}$$

The maximum kinetic energy the electron can gain is $E^{\rm max}_{\rm kin}(\theta_\gamma = \pi) = \frac{2\epsilon^2}{1+2\epsilon}\,m_e c^2$ which goes in the limit of $\epsilon \gg 1$ to $E^{\rm max}_{\rm kin}(\theta_\gamma = \pi) \to E_\gamma$.

4.1.3 Pair Production

In the electric field of a nucleus (another text book example) a photon with sufficient energy can convert into an electron-positron pair. The threshold energy is given by $E_\gamma \geq 2\,m_e c^2 + 2\,m_e c^2/m_{\rm target}$, leading to $E_\gamma \geq\approx 2\,m_e c^2$ for pair production on a nucleus, and $E_\gamma \geq 4\,m_e c^2$ for pair production on an electron.

The cross section for $E_\gamma \gg 20\,\mathrm{MeV}$ is given by

$$\sigma_{\mathrm{pair}} = 4\,\alpha\,r_e^2\,Z^2\,\left(\frac{7}{9}\ln\frac{183}{Z^{1/3}} - \frac{1}{54}\right)\ \ [\mathrm{cm}^2/\mathrm{atom}] \approx \frac{7}{9}\,\frac{A}{N_A}\,\frac{1}{X_0} \tag{32}$$

with the definition for X_0 from eq. 29.

4.2 Interaction of Neutrons

Neutrons are neutral particles; for their detection we have to use some indirect methods. Neutrons have to interact and the interaction has to produce charged particles, which can themselves be detected with previously discussed techniques.

For low neutron energies ($< 20\,\mathrm{MeV}$), interactions like $n+{}^6\mathrm{Li} \rightarrow \alpha+{}^3\mathrm{H}$ using LiI(Tl) scintillators, $n+{}^{10}\mathrm{B} \rightarrow \alpha+{}^7\mathrm{Li}$ using BF_3 filled gas counters, $n+{}^3\mathrm{He} \rightarrow p+{}^3\mathrm{H}$ using ^{3}He-filled proportional counters, and $n + p \rightarrow n + p$ using proportional chambers filled for example with for example CH_4, are used.

For high neutron energies ($> 1\,\mathrm{GeV}$), coated proportional counters to detect the fission products of $n + {}^{235}\mathrm{U}$ and hadron calorimeters (see section 11.2) are used.

4.3 Interactions of Neutrinos

Neutrinos and anti-neutrinos are directly detected with charged-current interactions: $\nu_e + n \rightarrow p + e^-$, $\overline{\nu_e} + p \rightarrow n + e^+$, $\nu_\mu + n \rightarrow p + \mu^-$, $\overline{\nu_\mu} + p \rightarrow n + \mu^+$, $\nu_\tau + n \rightarrow p + \tau^-$, $\overline{\nu_\tau} + p \rightarrow n + \tau^+$. The cross section is extremely small, for neutrinos of $0.5\,\mathrm{MeV/c}$ $\sigma(\nu_e N) = 1.6 \cdot 10^{-44}\,\mathrm{cm}^2$ For high energies (GeV range), the cross section is $\propto E_\nu$, $\sigma(\nu_\mu N) = 0.67 \cdot 10^{-38}\,E_\nu\,\mathrm{cm}^2/(\mathrm{nucleon\ GeV})$ and $\sigma(\overline{\nu_\mu} N) = 0.34 \cdot 10^{-38}\,E_\nu\,\mathrm{cm}^2/(\mathrm{nucleon\ GeV})$.

Usually indirect measurements of the neutrinos are performed with hermetic detectors, applying missing momentum and missing energy techniques.

5. Electromagnetic Cascades

As mentioned in section 2.6, for high electron energies the most probable process is Bremsstrahlung (eq. 28), e.g. the generation of a real photon. For high photon energies, the most probable process is pair creation (section 4.1.3, eq. 32). We can understand the basic features of the two processes playing ping-pong with a simple toy model. In every step t, which corresponds to one conversion, where the step size is related to the Radiation length X_0 (eq. 29), the number of particles N is doubled ($N(t) = 2^t$) and the energy E of each particle is halved ($E(t) = E_0 \cdot 2^{-t}$). The multiplication stops at $t_{\max}$, where the energy of the particle falls below a critical energy $E_c = E_0 \cdot 2^{-t_{\max}}$, which we can associate to the pair production threshold. For the position of the shower maximum we obtain

$$t_{\max} = \frac{\ln E_0/E_c}{\ln 2} \propto \ln E_0 \tag{33}$$

For the total number of shower particles S:

$$S = \sum_{t=0}^{t_{\max}} N(t) = \sum 2^t = 2^{t_{\max}+1} - 1 \approx 2 \cdot 2^{t_{\max}} = 2 \cdot \frac{E_0}{E_e} \propto E_0 \tag{34}$$

and for the total track length $S^\star$, measured in sampling steps t

$$S^\star = \frac{S}{t} = 2 \cdot \frac{E_0}{E_c} \cdot \frac{1}{t} \tag{35}$$

The energy Resolution is then given by

$$\frac{\sigma(E_0)}{E_0} = \frac{\sqrt{S^\star}}{S^\star} = \frac{\sqrt{t}}{\sqrt{2E_0/E_c}} \propto \frac{\sqrt{t}}{\sqrt{E_0}} \tag{36}$$

All basic features of electromagnetic showers are reproduced by this simple model: the position of the shower maximum is $\propto \ln E_0$, the number of shower particles is $\propto E_0$, and the energy resolution is $\propto 1/\sqrt{E_0}$.

A more realistic description of longitudinal shower development yields

$$\frac{dE}{dt} = \text{const} \cdot t^a \cdot e^{-bt} \tag{37}$$

where a, b a parameters which have to be determined for the specific detector material used.

The lateral spread of the shower, which is caused by multiple scattering, is given by the Molière Radius R_m,

$$R_m = \frac{21\,\text{MeV}}{E_c}\, X_0[\text{g/cm}^2] \tag{38}$$

which is defined so that $95\,\%$ of the shower energy is contained in a cylinder of radius $2\,R_m$. For a homogeneous calorimeters build out of iron $R_m^{\text{Fe}} = 1.8\,\text{cm}$, and out of lead $R_m^{\text{Pb}} = 1.6\,\text{cm}$.

6. Hadron Showers

The longitudinal development of hadron showers is governed by the nuclear interaction length λ_I (see section 3.), and the lateral development by the transverse momentum p_T of secondary particles. Since $\lambda_I > X_0$ and the average p_T from nuclear interactions is much larger than the average p_T from multiple scattering (eq. 7), hadron showers are wider and longer than electromagnetic showers of the same original energy.

Due to the multitude of possible processes during the shower creation, the hadron energy is transferred into several groups, each of them with their own systematic energy dependencies, and the distribution into the groups is subject to fluctuations. Part of the energy goes into charged particles, and if they are μ's, some of the energy is lost (or better: not detected). π^0's produced in the shower initiate an electromagnetic cascade, which is usually contained. Nuclear binding energy can be partially recovered by fission, but the energy in nuclear fragments will be partially lost. In general, the visible energy is systematically lower than the original particle energy, and due to the fluctuations in the losses the energy resolution of hadron calorimeters is worse than for electromagnetic calorimeters.

One important point to optimize the energy resolution is to balance the different responses to electrons and hadrons ($e/\pi = 1$, compensation). We will discuss this again in the section 11.2.

7. Drift and Diffusion in Gases

In this section we will discuss effects after particle lost it's energy and ionized the atoms or molecules of a gas.

The electrons and ions lose their energy by multiple elastic and inelastic collisions with the other atoms and molecules of the gas, and will shortly reach thermal equilibrium. The ionization cloud will diffuse and has a Gaussian width $\propto \sqrt{(}t)$, where t is here the time.

With an additional electric field, the cloud will drift with a constant velocity v_{drift}, which depends on the gas and the strength of the electrical field, but is usually measured in cm/μsec (example: argon-isobutane: $v_{\text{drift}}^{\text{electron}} \approx 5\,\text{cm}/\mu\text{sec}$). The longitudinal and transverse diffusion coefficients are different, due to the energy dependent electron-molecule cross section. The drift velocity is $v_{\text{drift}} \propto 1/m$, so ions drift several thousand times slower than electrons.

With an additional magnetic field, the drift will be under an angle due to the additional (velocity dependent) Lorentz force.

Part II: Basic Design of Detectors

In this part we will apply some of the physics discussed in the first part to examples of particle detectors. We will discuss wire chambers in several incarnations, which are usually used to measure the position of particles, and electromagnetic and hadron calorimeters, which are used (as already indicated by their name) to measure the total energy. In the third part we discuss specific detectors used to identify particles.

It is important to note that in general it is not possible to classify one detector type into one specific group; overlaps are common and useful so one detector can perform more than one specific task.

8. Wire Chambers

8.1 Ionization Chamber

This is the simplest gas detector, but also can be build with liquid or solid materials. It is basically a large capacitor, either flat or with cylindrical symmetry (a can with a wire in the center), where the ionization (electrons and ions) drift to anode and cathode resp. The moving charges can be collected, amplified and integrated over time, which will give a signal which is proportional to the original ionization loss.

8.2 Proportional Counters

This detector is usually build as a cylinder like an ionization chamber, but with a smaller diameter wire in the center or operated at a higher voltage (or both). Due to the higher field close to the surface of the wire, the electrons gain enough energy so they are able to ionize more of the counting gas molecules and produce an avalanche. This charge multiplication results in a higher induced current in the wire. The word *proportional* in the name stems from the fact that at not too high operating voltages the gas amplification is constant and the measured signal is proportional to the primary ionization.

8.3 Geiger-Müller Counter

This detector is build in the same geometry as the Proportional Counter, but operated at an even higher voltage. In the gas multiplication avalanche, in addition to ions also excited atoms and molecules are produced, where some of them de-excite via the emission of a photon. This leads to a copious production of photons, which can ionize more via the photoelectric effect (see section 4.1.1), also far away from the original avalanche.

Two possibilities are used to stop discharge. One is to make the resistor between the high voltage supply and the counter big enough, so every time the counter draws a lot of current, the voltage will drop. The other is to add alcohols, like methylal or ethyl-alcohol, or hydrocarbons, like methane, ethane, or isobutane, to the counting gas (usually argon); they will absorb the UV photons and reduce the free path for them.

8.4 Gas Multiplication

As seen in the previous sections, the same detector can be operated in different modes, and each of them carries its own name. At very low voltages (or electric fields), the ions and electrons will just recombine. At low voltages, the two charges are separated and we operate a ionization chamber. For medium voltage, we have constant gas amplification and are operating a proportional counter, and a high voltages, we operate in the Geiger-Mode. At very high voltage we will experience glow discharge, which can destroy the detector.

8.5 Multiwire Proportional Chambers

At the beginning of the 1960's, George Charpak (Nobel Price 1992) and others started to build detectors containing more than one counting wire, extending significantly the use of this kind of detectors. The advantage to the previously used bubble chambers is obvious: The signal is electric, so it can can easily be fed into electronics, which also started to be developed around that time.

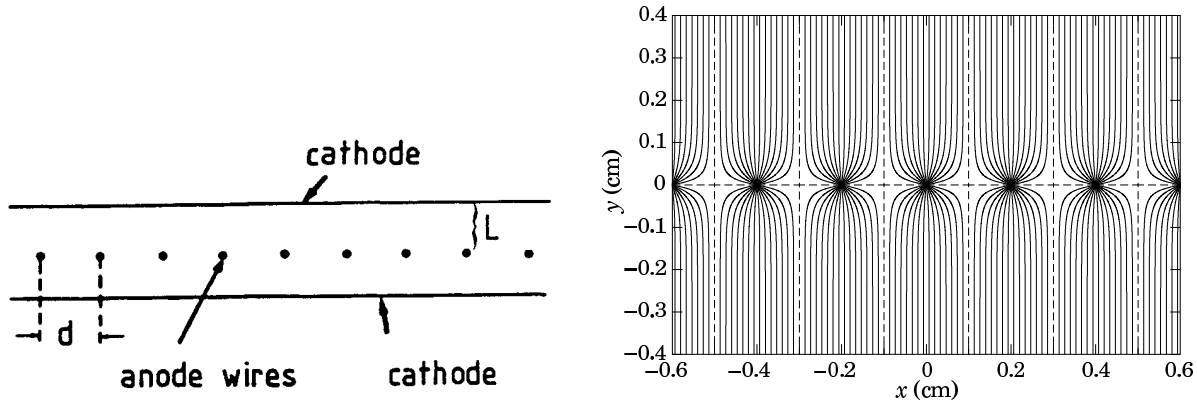

Fig. 3: Left: Side view of a Multiwire Proportional Chamber. Right: Electric field lines in a MWPC.

Over a (usually rectangular) frame, several wires are stretch in parallel. A cathode foil above and below the wire plane completes the detector. Typical dimensions are: wire distance d a few mm (smallest known to me $0.8\,$mm), wire diameter $10\,\mu$m $- 30\,\mu$m, thickness of chamber L a few wire distances, and total sizes up to square meters. The total size is limited by the wire tension and electrostatic repulsion.

The electric field lines form automatically cells, the electrons from ionization drift to the closest wire. The readout electronics consists of a simple discriminator sending a logical output whenever a particle passed close to that wire. The spatial resolution is $\sigma = d/\sqrt{12}$, but only in one dimension. A second, identical module, mounted under an angle, has to be used for the other dimension. Some detectors also use segmented cathodes for that.

8.6 Planar Drift Chambers

As mentioned above, wire chambers are limited by the electrostatic repulsion between wires, which requires a minimum distance as well as strong frames to stand the forces. At the middle of the 1960's, Heintze and Walenta [16], but also others, came up with a new idea: Keep the basic geometry of a MWPC, but make the wires further apart, and use the drift time of the electrons to the wire as additional information. As described in section 7., in an homogeneous electric field the drift velocity is constant. A start signal for measuring the drift time is usually readily available in an experiment, for example from a plastic scintillator (section 2.3) defining the incoming beam.

Drift distances over several centimeters can be easily achieved, and the resolution is limited by diffusion; In small chambers, $\sigma > 20\,\mu$m, in larger (square meter) chambers a few $100\,\mu$m can be obtained.

8.7 Cylindrical Drift Chambers / Jet Chambers

The same idea as in the planar drift chambers can be realized in a cylindrical geometry, more adapted to collider detectors. The wire will be (nearly) parallel to the beam pipe, and a magnet field parallel to the beam (so it will not disturb it) will curve the charged particles in a plane perpendicular to the beam direction, allowing the determination of the momentum and charge of the particles. Wires are arranged radially to the outside, and the detector looks like composed of pieces of pie in the r-ϕ view. The largest

chamber of this type is the Central Jet Chamber of the OPAL detector at LEP, with a radius of nearly 2 meters, and a length of 4 meters, containing about 3500 counting wires [10].

8.8 Time Projection Chamber

TPCs are another device which uses in a clever way drifting electrons in a gas counter. A big usually cylindrical volume (meters in diameter, meters in length) has a (thin) positive high voltage electrode in the center plane, forcing electrons to drift toward the end plates of the cylinder. To reduce the longitudinal diffusion of the electrons, a magnet field is in parallel with the electrical field, so electrons can only spiral around the magnet field lines. The end plates are equipped with wires and a segmented cathode plan taking a two-dimensional image of the arriving electrons; the third coordinate is obtained by measuring the drift time.

This detector was successfully used in the ALEPH experiment at LEP, but also is used in Heavy Ion experiments with extremely high track density, like in STAR at RHIC and, in preparation, for ALICE at LHC.

9. Solid State Tracking Detectors

9.1 Silicon Strip Detectors

In the 1980's, silicon microstrip detectors became used heavily in HEP. They are absolutely necessary to measure properties of particles containing charm and beauty quarks. Examples for very successful experiments using this kind of detectors include E691 at Fermilab, WA82 at CERN, and, in colliders, CDF, the 4 LEP experiments (Aleph, DELPHI, L3, OPAL), and the HERA experiments. Today there are a lot of experiments using silicon microstrips, with channel counts up to 1 million or more.

The detector allows to measure with a precision of down to a few μm the one-dimensional position of a passing charged track. Newer devices, the so-called pixel detectors, measure a two-dimensional position. The detector uses as basic detection device a pn-junction, shown in fig. 4 left, a diode which is

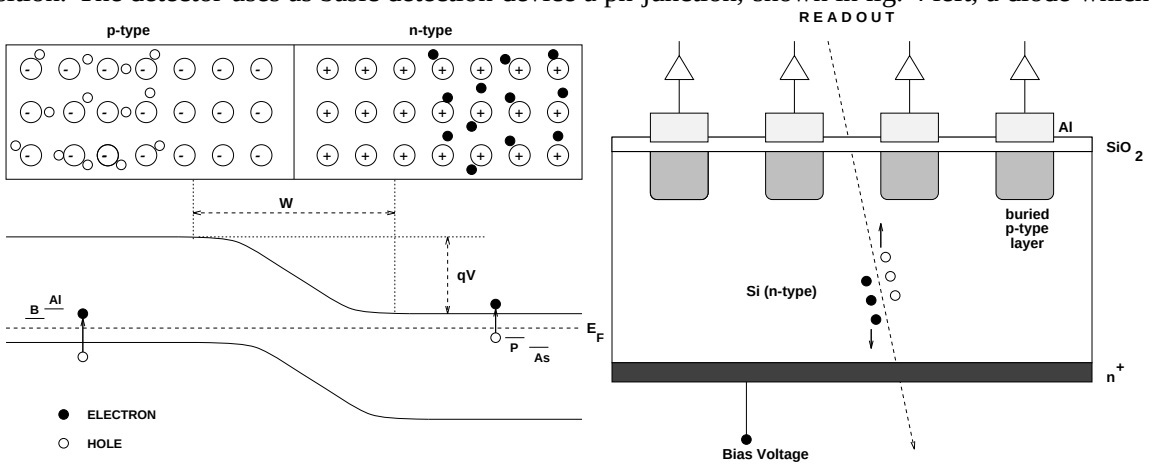

Fig. 4: Left: Model of a pn-junction in a semiconductor. Right: Schematic drawing of silicon strip detector. Both figures taken from [17].

operated in blocking direction with a sufficiently high voltage so that the entire device is depleted, e.g. there are no free electron-hole pairs (also called charge carriers). In one device several (thousands) of these pn-junctions are operated, arranged in parallel strips. Should a charged particle pass through the detector (see fig. 4 right), new electron-hole pair are created and one of the carrier types will drift toward

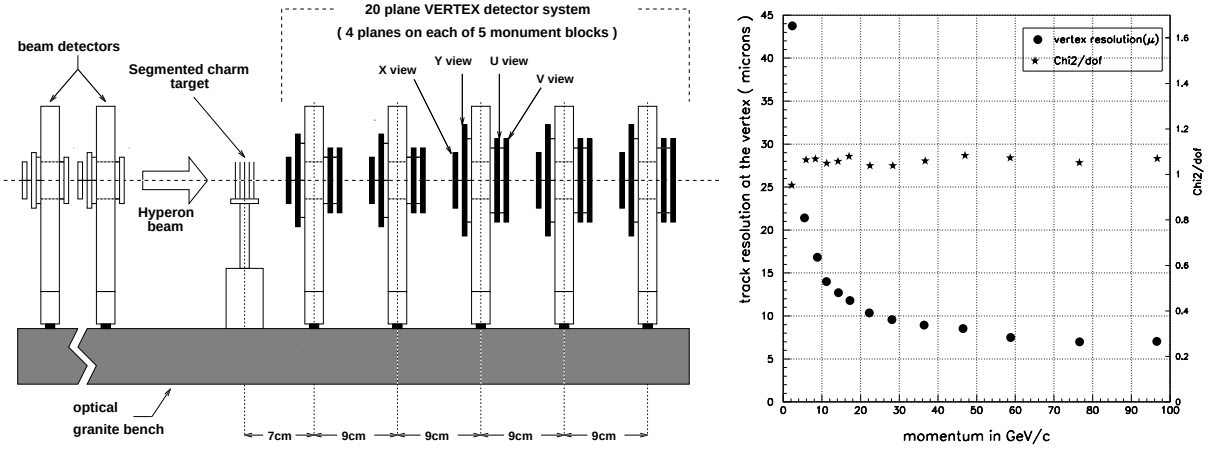

Fig. 5: Left: Layout of the SELEX vertex detector. After the target is a total of 20 planes with $20\,\mu$m and $25\,\mu$m strip distance in 4 orientations. Right: Mean χ^2/dof and vertex track resolution as a function of momentum. Figure taken from [17].

the nearest strip. In Silicon, the energy loss $dE/dx \approx 3.8\,\text{MeV/cm}$, and the energy needed to create one electron-hole pair is $3.6\,\text{eV}$[1], so in a typically $300\,\mu$m thick detector about $3 \cdot 10^4$ pairs will be created.

The construction of the detector itself seems to be under control today. There are several companies available which will produce the silicon detector with a well understood process. The smallest strip distance used today is $10\,\mu$m, so that the structure is actually much simpler than the achieved sub-micron structures in todays computer chips. The real challenge in these detectors is the readout: Imagine a $5\,\text{cm} \times 5\,\text{cm}$ detector with $10\,\mu$m strip distance: 5000 strips with their small signals have to be read out. Every single strip needs a preamplifier, and some kind of signal detection like a discriminator, otherwise noise will overwhelm the data acquisition. To reduce the number of cables (anyway, how to have a cable every $10\,\mu$m?) it would be nice to chain several channels together, at best even all 5000. The chips should then be clever enough only to send a strip number to the data acquisition, e.g. the signal gets digitized and zero suppressed already at the detector.

A system like this, called SVX [18], was developed about 10 years ago by LBL for collider experiments (CDF), and also used in WA89 [19] and SELEX [17, 20]. Never version are at use now in D0 (SVXII) and CDF (SVXIII).

The layout of a typical fixed target vertex detector is shown in fig. 5. Tracks originating from the targets are traversing the silicon planes oriented in 4 different orientations (rotated by $45°$) to allow the reconstruction of tracks in space. They eventually get fit to form a vertex, and the obtained resolution is shown in fig. 5 (right). At high momentum the resolution is limited by the strip distance, but at lower momentum multiple scattering becomes more and more important. Nevertheless, the fit takes all error contributions correctly into account, as seen from a constant $\chi^2 = 1$ for all momenta. There is a lesson to learn: more detectors is not always good.

9.2 Other Silicon Detectors

Other silicon detectors work on the same basic principles. Double-Sided strip detectors have a second strip structure on the back side of the silicon waver, with additional dotations to achieve the diode structure. The strips are usually, but not always, under $90°$. The readout is more complicated, two orthogonal sides have to have readout contacts, and in general double sided silicon is noisier and more difficult to operate. The signal is still not a real 3d information, pattern recognition algorithms have to be used to assign hits in a multi-track environment. The main advantage is the reduction of multiple scattering,

[1] The band gap in Silicon is only 1.1 eV, but Silicon is an indirect semiconductor.

since one waver can be used to measure two projections.

Silicon Drift detectors follow the same idea as wire drift chambers: use the time information to reduce the number of readout channels. This kind of detector will be used in the ALICE detector [21].

Silicon Pixel Detectors have, as says the name, no strips, but usually rectangular pixels, and give real 3d information of the passing tracks. The bonding process for the readout electronics is very complicated, but doable, as the prototypes for the BTeV experiment show [22]. The real 3d information is a key ingredient for the information to be used in the trigger.

10. Photomultipliers

Photomultipliers convert light (photons) via the photoelectric effect (see section 4.1.1) to an electrical signal. The original photo-electrons (in the most extreme case only one) is multiplied by accelerating the electron(s) in an electric field, hitting a metallic surface and thereby releasing more electrons, in several stages; multiplication factors of 10^5 or more can be obtained.

The efficiency to detect a photon depends on its wavelength and on the photo-cathode material, and has a typical maximum of up to 25%. The photo-cathode material has to be adopted to the emission

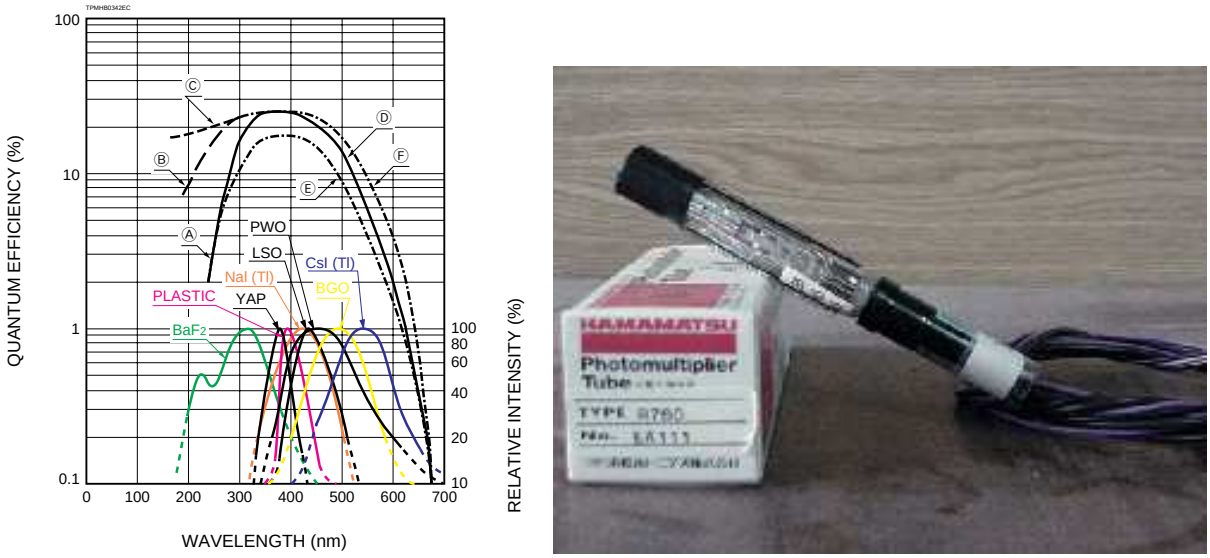

Fig. 6: Left: Emission spectra for different photon sources, with the quantum efficiency for different photo-cathode materials [23]. Right: Photo of a Hamamatsu R760 1/2 inch photo-multiplier tube.

spectrum of the photons to be detected, as shown in fig. 6.

Phototubes are distinguished by their diameter (available from 3/8 inch to ≈ 40 cm), and the number of multiplication stages (between 5 and 15). The entrance window can be on top ("head on") or on sides ("side on"). Good summaries about photomultiplier properties can be found in [23, 24].

11. Energy Measurement: Calorimeters

The shower of an electromagnetic or hadronic cascade has to be totally absorbed. If not, the resolution will be reduced due to fluctuations in the leakage. For electrons and photons (section 5.) the sizes needed are governed by the Radiation Length X_0 (eq. 29), while for hadrons (section 6.) they are governed by the Interaction Length λ_I. Different optimizations have to be adopted for electrons/photons and hadrons. In addition, for a hadron calorimeter we have to take into account the electromagnetic part of the showers due to π^0's, which requires the concept of "compensation" [4]. A linear dependence on the

original particle energy of the output signal can usually be achieved. The relative energy resolution is $\sigma(E)/E \propto 1/\sqrt{E}$, while the shower maximum is a logarithmic function of the energy.

11.1 Electromagnetic Calorimeters

We can distinguish two basic designs: A sampling calorimeter, which we will discuss in more detail in section 11.2, and a homogeneous calorimeter. The latter comes in two groups: one using the scintillation properties of matter (section 2.3), for example CsI crystals, and one measuring the amount of Cherenkov light (section 2.4) produced in a dense but transparent material like lead-glass. The lateral segmentation is about one Moliere Radius R_M (eq. 38), and the depth has to be sufficient to contain the full shower. Each block of material has a photomultiplier attached at the end; in the case of the ionization loss measurements, ionization chambers are immersed into the liquids. Successful Calorimeters include WA89 Lead-class calorimeter [25], the KTeV CsI calorimeter [26], and the BGO Calorimeter of L3 [27].

11.2 Sampling Calorimeters

A sampling calorimeter has 2 parts: Something "heavy", inactive, like lead, uranium, iron (steel), and something "light", active, like plastic scintillator (section 2.3), wire chamber (section 8.5), liquid (ionization chamber). The two materials are either put together is an alternating multilayer sandwich or mixed together, like lead or iron tiles with scintillating fiber readout.

The main design choices is how to use the thicknesses, relative and absolute, of the two materials. Problems to consider are: The inactive part absorbs some of the produced shower particles, and the absorption fraction is different for hadrons and electrons; some part of the hadronic response is lost due to neutron absorption; all hadronic showers have an electromagnetic component due to the π^0's produced in the cascades, and the obtained responses e.g. the physics effects, are different.

The electromagnetic part was understood long time ago and good simulation software (EGS) was and is available as part of the GEANT (see section 13.) package. Only in the 1980's, first systematic studies for hadronic responses were performed. The first tries led to a Uranium / Scintillator sandwich calorimeter, of which a first prototype had a surprisingly (for that time) good resolution. The only partly correct explanation brought up was that fission gives back some of "lost" neutron energy. As was found out later, the first prototype was "compensated" by accident.

In the mid-1980's, systematic studies on hadronic shower profiles and absorptions were started by Wigmans et al. A good account of this history is the book by Wigmans [4]. The results of these studies was that *any* material combination can be tuned to give identical responses to electrons and hadrons ("compensate"), due to the different dependencies on Z of the physics processes involved. The best resolution for hadrons can only be achieved if the calorimeter is compensated. This understanding helped to improve the resolution for hadronic showers, which was before typically$\sigma_E/E \approx 100\,\%/\sqrt{E}$ to the best achieved values of $30 - 35\,\%/\sqrt{E}$.

12. Some words about Electronics

Electric signals from detectors are small and fast. This requires high frequency, high bandwidth, low noise electronics, which are not totally compatible requirement to easily design the electronics. In addition, the detector capacitance is usually big, and noise is often $\propto C^2$. All noise sources (shot noise (leakage current), thermal noise, $1/f$ noise) have to be analyzed with great care. Stray capacitances and inductances on printed circuits are significant at high frequencies ($\geq$ 100 MHz) and have to be taken into account during the layout of a board, as well as the finite signal speed ($\sim$ 5 cm/nsec). All these problems indicated here require a much more detailed study as can be provided here. A first start for further reading is the electronics section of the Particle Data Book [6].

13. Some words about Simulation

Detectors are complex, complicated and expensive to build. Within one sub-detector and different sub-detectors of an experiment interferences, which seem to be mostly destructive, are possible. Long before building even prototypes, simulations of parts or full behavior and responses of sub-detectors or full detectors is absolutely necessary. The software tool used for these tasks is GEANT [28]. This software package includes models all interactions of all particles, which can selectively be switch on or off. The distribution of material is given as a start, and GEANT is doing everything else. The original versions were written in FORTRAN, the preferred language of particle physicists. The documentation is extensive, and also can serve as a summary of the modeling of physics processes. Unfortunately, for complex geometries simulating can be very slow, and it is often necessary to parametrize the response of detectors.

Part III: Particle Identification

Here we will discuss as an example for the application of the detectors described up to now, the identification of particles. We will discuss in more detail transition radiation detectors and Cherenkov detectors.

To identify neutral particles, we can only measure their total energy and, if no charged track is pointing to the signal in the calorimeter, conclude that this was a neutral particle. Usually not too many possibilities are left; for example in a hadron calorimeter, the only choices are neutrons or K_L^0's.

In an electromagnetic calorimeter, one can measure in addition "E/p", e.g. the deposited energy over the previously measured momentum of a charge particle. If $E/p = 1$ we have a (relativistic) electrons, $E/p < 1$ for hadrons, and if E/p is compatible with minimum ionization, we have a muon.

Long-lived neutral particles like the hyperons Λ^0 and Ξ^0, and short lived (but still weakly decaying) particles (τ, charm, beauty), we have to measure the 4-vector of all decay products to be able calculate the invariant mass of the final state.

The second major applications is the identification of beam particles for Fixed Target experiments. In both cases, the momentum of the particle is known, in the case of neutral particles by guessing, for charged particles by direct measurement in the beam line or by a magnetic spectrometer. With this in mind, particle identification reduces to measure some additional quantity, like to total energy with a calorimeter, or some velocity (β) dependent effect like time-of-flight (section 14.), dE/dx (eq. 18), Cherenkov (section 2.4) or Transition Radiation (eq. 26).

14. Time–of–flight (TOF)

This is the simplest method for identifying particles: Put two scintillation (or gas) counters at a known distance and measure the time difference between the two signals. Time resolutions of about 150 psec can be achieved, and with the maximum distance possible between the two detectors (≈ 10 m for measuring decay products, ≈ 100 m in a beam line) kaons and pions can be separated up to a few GeV$/c$. At higher rate and/or more than one particles hitting the same detector elements the time difference measurement is ambiguous and the method will not work anymore.

15. Transition Radiation Detectors (TRD)

The physics behind these detectors was discussed in section 2.5. The detection of Transition Radiation is complicated by the fact that the X-rays are emitted under a small angle with respect to the particle track (eq. 26), so in a detector the X-ray and the dE/dx signal are seen together and are of the same order of magnitude. In addition, the dE/dx signal is Landau distributed, forcing the use of several $(10 - 30)$ radiator stacks and chamber (with heavy gases like Xenon or Krypton) units to be able to distinguish the two signals[29, 30, 31, 32].

Some detectors exploit the fact that the ionization due to the X-ray is more point-like (photoelectric effect), as opposed to the more equally distributed dE/dx signal. The Charge Integration method measures the total charge of the ionization in every unit, and counts how many chambers saw a total charge larger than some given threshold. The Cluster Counting method employs the different spatial ionization distribution of the two source (point for X-ray, line for dE/dx) to separate them. The obtained signals (either clusters or charge) are compared with a likelihood method to differentiate particle hypothesis, with known momentum. The most probable hypothesis is selected as the result of the identification.

The most extreme and sophisticated usage of TRD technology is planned for the ATLAS experiment at the LHC. They will use more than 370,000 straw tubes as transition radiation detector and in addition use the obtained information for tracking [33].

16. Cherenkov Detectors

16.1 Threshold Cherenkov Detectors

With a suitable medium, which has an refractive index where one of the particles is above and the other below the threshold (eq. 22) to produce Cherenkov light, these detectors are used in fixed target beam lines to separate two particles with the same (fixed) momenta.

For the identification of decay products over a wider momentum range, and/or if more than two particles have to be distinguished, several counters at different thresholds have to be employed. Since each of them is typically several meters long, in practice not more than three are used. The combination of signals for different momentum ranges yields a decent identification probabilities.

16.2 Ring Imaging Cherenkov Detectors (RICH)

Even though the basic idea of determining the velocity of charged particles via measuring the Cherenkov angle was proposed in 1960 [34], and in 1977 a first prototype was successfully operated [35], it was only during the last decade that Ring Imaging Cherenkov (RICH) Detectors were successfully used in experiments. A very useful collection of review articles and detailed descriptions can be found in the proceedings of four international workshops on this type of detectors, which were held in 1993 (Bari, Italy) [36], 1995 (Uppsala, Sweden) [37], 1998 (Ein Gedi, Israel) [38], and 2002 (Pylos, Greece) [39], respectively. In 2004 the workshop will be held in Mexico [40].

By measuring the Cherenkov angle θ one can in principle determine the velocity of the particle, which will, together with the momentum p obtained via a magnetic spectrometer, lead to the determination of the mass and therefore to the identification of the particle.

Neglecting multiple scattering and energy loss in the medium, all the Cherenkov light (in one plane) is parallel, and can therefore be focused (for small θ) with a spherical mirror (radius R) onto a point. Since the emission is symmetrical in the azimuthal angle around the particle trajectory, this leads to a ring of radius r in the focus, which is itself a sphere with radius $R/2$. The radius r is given by

$$r = \frac{R}{2}\tan\theta \approx \frac{R}{2}\sqrt{2 - \frac{2}{n}\sqrt{1 + \frac{m^2c^2}{p^2}}} \tag{39}$$

16.2.1 A Short History of RICHes

After the first successful laboratory tests in the 1970's [35], at the beginning of the 1980's the first generation of Ring Imaging Cherenkov Detectors were built, with mixed results. Examples are the CERN Omega RICH, used by WA69 and WA82 [42], the UA2 RICH at CERN, and the E653 RICH at Fermilab.

A second generation RICH detectors were developed and employed at the end of the 80's and beginning of the 90's, with the positive and negative experiences from the first generation incorporated. Examples are an upgraded Omega RICH, used by WA89 and WA94 [42], Delphi, CERES (all at CERN), and the SLD–GRID at SLAC. All these detectors had significant startup problems to overcome, but eventually they all worked very well and contributed to the physics analysis of the experiments.

The third generation, build and used mid-end 90's, finally worked without too many problems from the beginning and all of them played an important role in the physics analysis. Examples are the SELEX RICH at Fermilab, and Hermes and Hera-B at DESY.

Since the mid-90's, the RICHes are an established detector type, and are currently employed in recent experiments: BaBar–DIRC (SLAC), PHENIX and STAR (Brookhaven-RHIC), CLEO–III (Cornell), COMPASS (CERN).

There is a long list of future experiments, who plan to or are already building RICHes: ALICE, LHCB (CERN), BTeV, CKM (Fermilab), and many more. Also in other fields like nuclear physics (GSI)

and in astroparticle physics experiments technology developed for RICHes is used.

16.2.2 General Details for RICHes

Since the number of photons is $\propto \lambda^{-2}$ (eq. 25), most of the light is emitted in the VUV range. To fulfill equation 23, the refractive index has to be $n > 1$, so there will be no Cherenkov radiation in the x-ray region. Also it is very important to remember that n is a function of the wavelength ($n = n(\lambda)$, chromatic dispersion) and most materials have an absorption line in the VUV region, where $n \to \infty$. Since usually the wavelength of the emitted photon is not measured, this leads to a smearing of the measured ring radius, and one has to match carefully the wavelength ranges which one wishes to use: Lower wavelengths gives more photons, but larger chromatic dispersion.

A very useful formula is obtained by integrating eq. 25 over λ (or E), taking into account all efficiencies etc., obtaining a formula for the number of detected photons N_{ph} [35]:

$$N_{\mathrm{ph}} = N_0 L \sin^2\theta \tag{40}$$

where N_0 is an overall performance measure (quality factor) of the detector, containing all the details (sensitive wavelength range, efficiencies), and L is the path length of the particle within the radiator. A " very good" RICH detector has $N_0 = 100\,\mathrm{cm}^{-1}$, which gives typically around 10 to 15 detected photons (N_{ph}) per $\beta = 1$ ring.

The usual construction of a RICH detector is to use a radiator length of $L = R/2$, e.g. the path length is equal to the focal length; but any other configurations, like folding the light path with additional (flat) mirrors, are possible.

All the presented arguments only work for small θ, which is always fulfilled in gases, since n only differs little from 1. Also important is the fact, that, should the particles not pass through the common center of curvature of mirror(s) and focal spheres, the ring gets deformed to an ellipse or, in more extreme cases, to a hyperbola. If the photon detector is able to resolve this, and the resolution is needed for the measurement, these deviations from a perfect circle have to be taken into account in determining the velocity β. In general this effect can be neglected, and all parallel particles (with the same β) will give the same ring in the focal surface, due to the fact that all emitted Cherenkov light is parallel. The position of the ring center is determined by the angle of the tracks, not by their positions.

In the following, we will describe three RICH detectors used in experiments, and a new application for RICH detectors for a new experiment.

16.2.3 The CERN Omega-RICH

In the middle of the 1980's, first attempts were made to apply the prototype results obtained by Séguinot and Ypsilantis [35] to experiments in a larger scale. One of these attempts was performed at the CERN Omega facility in the West Hall. Experiments WA69 and WA82 tried to use this detector for their analysis, but only succeeded partly. An overview about this history can be found in [42]. When in 1987 a new experiment, later named WA89, was proposed [43, 44], an important part was a necessary upgrade of this detector for the use by this new experiment. Two main parts where changed: New photon detectors using TMAE as photon sensitive component, and new mirrors to perform the focusing. Details about the detector can be found in [42, 45, 46].

The overall layout of the detector shows that RICH detectors are basically simple devices: a big box, some mirrors at the end, and photon-sensitive detectors at the entrance. The real challenge is to combine all the parameters together to obtain a perfect match for the overall system.

The size of the radiator box and the photon detector is given by the angular distribution of tracks which have to be identified at the location of the detector. Since usually this detector is placed behind a magnetic spectrometer, and the momentum spectrum of the interesting tracks depends on the physics

goals of the experiment, the surfaces to cover have to be determined for every setup and experiment, usually with Monte Carlo simulations during the design phase of the experiment. In the case of WA89 [45], the mirror surface needed was about $1\,\mathrm{m} \times 1.5\,\mathrm{m}$, much smaller than the $4\,\mathrm{m} \times 6\,\mathrm{m}$ covered by the original Omega-RICH. It was therefore decided to replace only the central mirrors with smaller, higher surface quality mirrors to obtain better resolution.

The detector surface was calculated to be $1.6\,\mathrm{m} \times 0.8\,\mathrm{m}$, with a spatial resolution of a few millimeters for every detected photon. The pixel size could therefore not be much bigger than also a few millimeters, leading to about 100000 pixels in the detector plane. The solution was to build drift chamber (see section 8.6) (TPC) modules, covering an area of $35\,\mathrm{cm} \times 80\,\mathrm{cm}$, and approximating the focal sphere with a polygon of 5 modules. After passing a $3\,\mathrm{mm}$ thick (to minimize absorption) quartz window, the photons are absorbed by Tetrakis(dimethylamino)-ethylen (TMAE) molecules, converting via photo-effect (section 4.1.1) into a single electron. TMAE is present with a concentration of about $0.1\,\%$ within the driftgas, which is otherwise pure Ethan. Due to the use of a quartz window together with TMAE as photon-sensitive gas the detector is only sensitive in a small wavelength range between $165\,\mathrm{nm} < \lambda < 230\,\mathrm{nm}$. TMAE has a very low vapor pressure, so that at ambient temperatures the molecules are saturated within a gas. To obtain a short enough conversion length of around $1\,\mathrm{cm}$ (otherwise the conversion would occur to far away from the focal plane and lead to an additional contribution to the resolution (parallax)), the drift gas (Ethan) is led through a bubbler, containing TMAE liquid at 30° C. This means that everything after the bubbler, e.g. the whole detector including radiator box, had to be heated to 40° C to avoid condensation. Other unpleasant properties of TMAE include a high reactivity with Oxygen, producing highly electro-negative oxides, which will attach an electron easily, changing the drift velocity by a factor of several thousand, leading to a loss of electrons. Since the signal is a single electron (photo-effect!) this is catastrophic. The counting gas had an Oxygen contents of $< 1\,\mathrm{ppm}$.

Mostly due to the presence of TMAE, the operation of this detector was not trivial. All parameters were monitored electronically, and hardware limits on some critical parameters (like temperature, Oxygen content of Ethan) lead to a automatic shutdown of the detector, waiting for an expert to arrive in the experimental hall.

Once the electron was released, it was drifting under the influence of an electric field of $1\,\mathrm{kV/cm}$ (drift velocity $5.4\,\mathrm{cm}/\mu\mathrm{m}$) upwards or downwards over maximal $40\,\mathrm{cm}$ toward $6\,\mathrm{cm}$ long counting wires (gold-coated tungsten, $15\,\mu\mathrm{m}$ diameter), spaced by $2.54\,\mathrm{mm}$. The two-dimensional spatial information about the conversion point of the photon is obtained with the position of the wire and the drift time of the electron. In total, 1280 wires were used in the detector. An additional complication was that the charged particles itself were passing through the chambers, leaving a dE/dx signal of several hundred electrons, which is to be compared to the single electron which is our signal. This leads to increased requirements for the wire chambers (sensitive, e.g. sufficient multiplication, to single electrons, but no sparking with several hundred electrons) and to the preamplifier electronic (not too much dead time after a big pulse).

The overall resolution allowed the separation of pions and kaons up to a momentum of about $100\,\mathrm{GeV}/c$, which was exactly the design goal. This led to a good number of physics results (about 15 papers), which would not have been possible to obtain without the RICH detector.

16.2.4 The SELEX Phototube RICH Detector

At Fermilab a new hyperon beam experiment, called SELEX, was proposed in 1987 [48]. The key elements to perform a successful charmed-baryon experiments are 1) a high resolution silicon vertex detector and 2) a extremely good particle identification system based on RICH. During the following years, a prototype for the SELEX RICH was constructed and tested successfully [49], based in some part on experience gained by our Russian collaborators [50]. The real detector was constructed in 1993-1996, ready for the SELEX data taking period from July 1996 to September 1997. Details and performance descriptions of this detector can be found in [15].

Fig. 7: The SELEX RICH detector. The vessel has an overall length of a little over $L = 10\,\mathrm{m}$, the mirrors have a radius of $R = 1982\,\mathrm{cm}$, and the light tight box containing the photomultipliers is clearly seen on the left. The whole vessel is tilted by 2.4° to avoid that the particle trajectories go through the photomultipliers.

A photo of the detector is shown in fig. 7. The radiator gas is Neon at atmospheric pressure and room temperature, filled into the vessel with a nice gas-system [51]: First the vessel is flushed for about 1 day with CO_2 (a cheap gas). After this the gas (mostly CO_2 and little air) is pumped in a closed system over a cold trap running at liquid Nitrogen temperature, freezing out CO_2 and the remaining water vapor. At the same time Neon gets filled into the vessel to keep the pressure constant. This part of the procedure takes about 1/2 day, and the vessel contains afterward only Neon and about $100\,\mathrm{ppm}$ of Oxygen which is removed by pumping the gas over a filter of activated charcoal for a few hours, ending with an Oxygen contents of $< 10\,\mathrm{ppm}$ in the radiator. After this all valves were closed and the vessels sits there for the whole data taking of more than 1 year at a slight ($\approx 1\,\mathrm{psi}$) over-pressure.

The mirror array at the end of the vessel is made of $11\,\mathrm{mm}$ low expansion glass, polished to an average radius of $R = (1982 \pm 5)\,\mathrm{cm}$, coated with Aluminum and a thin over-coating of MgF_2, which gives $> 85\,\%$ reflectivity at $155\,\mathrm{nm}$. The quality of the mirrors was measured with the Ronchi technique [52] to assure a sufficient surface quality of the mirrors. The total mirror array covers $2\,\mathrm{m} \times 1\,\mathrm{m}$ and consists of 16 hexagonally shaped segments. The mirrors are fixed with a 3-point mount consisting of a double-differential screw and a ball bearing to a low mass honeycomb panel. The mirrors are mounted on one sphere, and were aligned by sweeping a laser beam coming from the center of curvature over the mirrors.

The photo detector is a hexagonally closed packed 89×32 array of 2848 half-inch photomultipliers. In a $3\,\mathrm{in.}$ thick aluminum plate holes are drilled from both sides, a $2\,\mathrm{in.}$ deep straight hole holds the photomultiplier, and a conical hole on the radiator side holds aluminized Mylar Winston cones, which form on the radiator side hexagons, leading to a total coverage of the surface. The 2848 holes are individually sealed with small quartz windows. For the central region of the array, a mixture of Hamamatsu R760 (fig. 6) and FEU60 tubes were used, in the outside rows only FEU60 tubes are present. The nearly 9000 cables (signal, hv, ground) are routed to the bottom (hv) or top, where the signal cables are con-

nected to preamp-discriminator-ecl-driver hybrid chips and finally readout via standard latch modules[2].

The SELEX RICH demonstrated a clear multitrack capability and low noise. To analyze an event, the ring center is predicted via the known track parameters, and a likelihood analysis [53] for different hypothesis (the momentum is known!) is performed to identify the particle. The final performance of this detector was evaluated [15]. The detector is nearly $100\,\%$ efficient for protons; even below the proton threshold the efficiency is above $90\,\%$. In the SELEX offline analysis, the RICH is one of the first cuts applied to extract physics results.

Up to date, SELEX published 10 papers with physics results from charm and hyperon physics, three of them in PRL.

16.2.5 DIRC at BaBar

BaBar is an experiment at SLAC, one of the so-called B-Factories, which are measuring in great detail $\mathcal{CP}$-violation parameters in B-Mesons. They employ a RICH detector which they call DIRC (Detection of Internally Reflected Cherenkov light) [54].

The radiator in this case are quartz bars, which, by internal reflection, transport the Cherenkov light to one side (the other side is mirrored). A standoff box, filled with water, expands the light and couples it to about 10,000 photomultiplier tubes. Due to the multiple internal reflections, the primary images are not rings, but present a more complicated pattern. Nevertheless, by considering in addition the arrival time of the photons at the PMTs, the Cherenkov angle can be reconstructed.

The performance of the DIRC is also very good. They reported high kaon efficiency and a low miss-identification probability. More information can be found in [55].

16.2.6 Future of RICHes with a Mexican touch: CKM

In 2001, a new experiment called CKM [56] received Stage I approval at Fermilab. The goal of the experiment is to measure the branching ratio for $K^+ \to \pi^+ \nu\bar{\nu}$ to an accuracy of $10\,\%$ (SM prediction is 10^{-10}) to measure the CKM matrix element V_{td}, contributing to test the Standard Model hypothesis that a single phase in the CKM matrix is the sole source of $\mathcal{CP}$ violation. To withstand the high expected physics background, the experiment will use, in addition to a conventional magnetic spectrometer, a velocity spectrometer consisting of two phototube RICH detectors, one to measure the incoming K^+, the second the outgoing π^+ [57]. The experiment is expected to take data in the second half of this decade.

The expected ring radii for K^+ and π^+ from the beam, measured in the Kaon RICH, are very well separated, so the usual resolution question is not appropriate to ask. The real question is: how Gaussian is the response function? The result, checked with SELEX single track data, using the standard SELEX algorithm, is that the response function is Gaussian over nearly 5 orders of magnitude.

16.2.7 Testing Cherenkov Mirrors

The HEP group in San Luis Potosí, Mexico is involved in the design, construction, and testing of parts of for the CKM RICH detectors. We will mention here especially the construction and testing of mirrors. We apply the Ronchi method [52]. The radius of a mirror is calculated from the distance of lines from a grating projected to the mirror surface. We are currently testing the first prototype mirrors produced in Mexico.

17. Summary Particle Identification

As a summary, we show in fig. 8 how to use different detectors to separate particles. Incidentally, in a fixed target experiment in a linear sense, and in a collider detector radial, this is the order of detectors the

[2] Since the phototubes are detecting single photons, no ADCs are necessary.

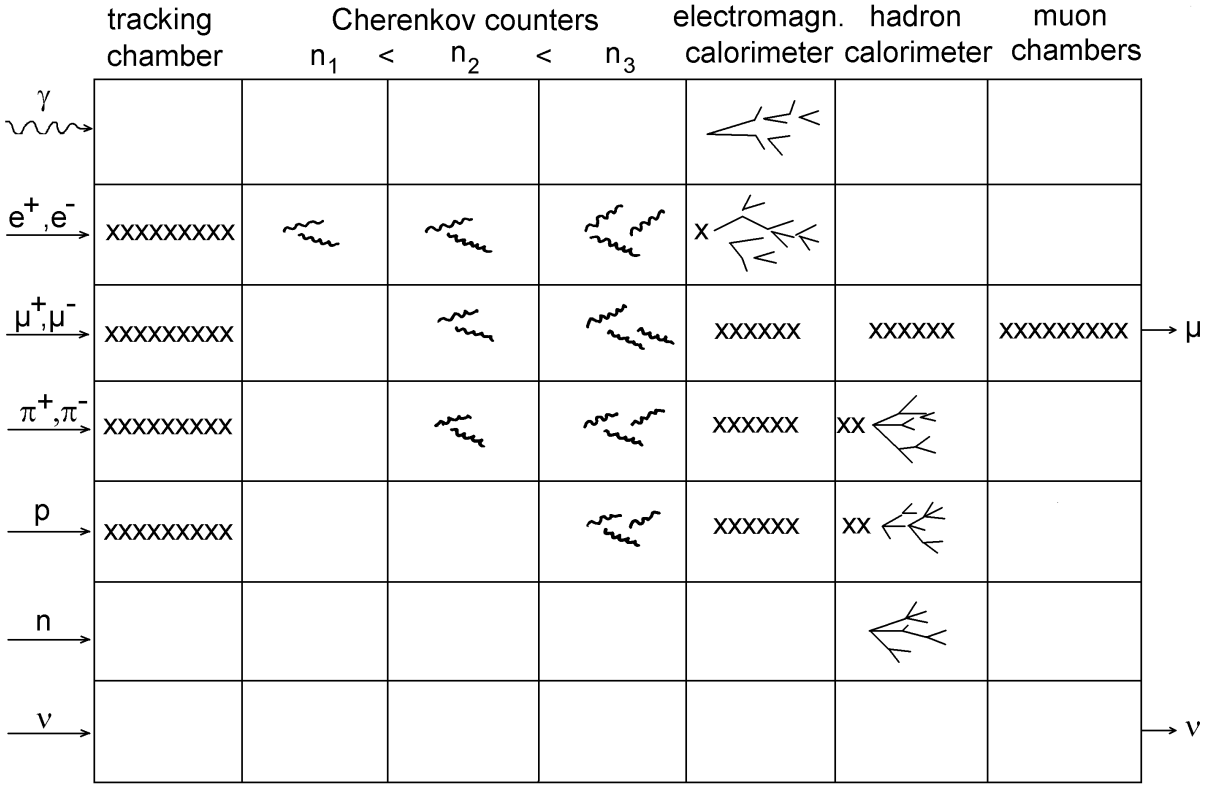

Fig. 8:

particles pass through.

18. Acknowledgment

The author thanks the organizers of this school for the invitation and the privilege to give a course on his favored topic.

References

[1] Claus Grupen: *Particle Detectors.* Cambridge University Press (2000).

[2] Konrad Kleinknecht: *Detectors for particle radiation.* Cambridge University Press, 2nd edition (1998).

[3] Richard C. Fernow: *Introduction to experimental Particle Physics.* Cambridge University Press (1986).

[4] Richard Wigmans: *Calorimetry.* Oxford Science Publishing (2000).

[5] C.W. Fabjan, J.E. Pilcher (Eds.): *Instrumentation in Elementary Particle Physics. Proceedings, ICFA School, Trieste, Italy, June 8-19, 1987.* World Scientific (1988).
J.C. Anjos, D. Hartill, F. Sauli, M. Sheaff (Eds.): *Instrumentation in Elementary Particle Physics. Proceedings, 3rd ICFA School, Rio de Janeiro, Brazil, July 16-28, 1990.* World Scientific (1992).
G. Herrera Corral, M. Sosa Aquino (Eds.): *Instrumentation in Elementary Particle Physics. Proceedings, 7th ICFA School, Leon, Mexico, July 7-19, 1997.* AIP Conference Proceedings 422 (1998).

S. Kartal, (Ed.): *Instrumentation In Elementary Particle Physics. Proceedings, 8th ICFA School, Istanbul, Turkey, June 28-July 10, 1999.* AIP Conference Proceedings (2000).
L. Villaseñor, V. Villanueva, (Eds.): *Instrumentation in Elementary Particle Physics. Proceedings, 1st ICFA Instrumentation School, Morelia, Mexico, November 18-29, 2002.* AIP Conference Proceedings 674 (2003).

[6] K. Hagiwara et al.: Physical Review **D66** (2002), 01001-1. `http://pdg.lbl.gov`

[7] Particle Data Group, to be published (2004). `http://pdg.lbl.gov`

[8] D.R. Nygren, J.N. Marx: *The Time Projection Chamber.* Phys. Today **31**, 46 (1978).

[9] J. Heintze: *The Jet Chamber of the JADE Experiment.* Nucl. Instrum. Meth. **196** 293-297 (1982).

[10] H.M. Fischer et al.: *The OPAL Jet Chamber Full Scale Prototype.* Nucl. Instr. Meth. **A252** (1986) 331-342.
H. Breuker et al.: *Particle Identification with the OPAL Jet Chamber in the Region of the Relativistic Rise.* Nucl. Instr. Meth. **A260** (1987) 329.
R.D. Heuer, A. Wagner: *The OPAL Jet Chamber.* Nucl. Instr. Meth. **A265** (1988) 11-19.

[11] K. Michaelian, A. Menchaca-Rocha, E. Belmont-Moreno: Nuclear Instruments and Methods **A356**, 297-303 (1995).

[12] P.A. Cherenkov: *Visible radiation produced by electrons moving in a medium with velocities exceeding that of light.* Phys. Rev. **52** (1937) 378.
Pavel A. Cherenkov, Ilja M. Frank, Igor Y. Tamm, Nobel Price 1958.

[13] I. Frank, I. Tamm: *Coherent visible radiation of fast electrons passing through matter.* C. R. Acad. Sci. URSS **14** (1937) 109.

[14] A. Satpathy et al.: BELLE Collaboration, hep-ex/9903045.

[15] J. Engelfried et al.: Nucl. and Instr. and Methods **A502** 62-65 (2003).
J. Engelfried et al.: *The SELEX Phototube RICH Detector.* Nucl. Instr. and Meth. **A431** (1999) 53-69. hep-ex/9811001.
J. Engelfried et al.: *The E781 (SELEX) RICH Detector.* Nucl. Instr. and Meth. **A409** (1998) 439.
J. Engelfried et al.: *The RICH Detector of the SELEX Experiment.* Nucl. Instr. and Meth. **A433** (1999) 149.
J. Engelfried et al.: *SELEX RICH Performance and Physics Results.* Nucl. Instr. and Meth. **A502** (2003) 285-288. Preprint UASLP-IF-02-007, hep-ex/0208046

[16] A.H. Walenta, J. Heintze, B. Schürlein: Nucl. Instr. Meth. **92** (1971) 373.

[17] P. Matthew: *Construction and Evaluation of a high Resolution Silicon Microstrip Tracking Detector and Utilization to determine Interaction Vertices.* Ph.D. Thesis, Carnegie-Mellon University, Pittsburgh (1997).

[18] S.A. Kleinfelder et al.: Lawrence Berkeley Laboratory Note.

[19] W. Brückner et al.: *Silicon μ-strip detectors with SVX-chip readout.* Nucl. Instr. Meth. **A348** (1994) 444-448.

[20] J. Russ, et al.: IEEE Trans. Nucl. Sci. **NS36** (1989) 471.

[21] V. Bonvicini, et al.: *Silicon Drift Detectors in the ALICE Experiment.* In: Ayala, Contreras, Herrera (Eds.): *Particles and Fields, Seventh Mexican Workshop.* AIP Conference Proceedings 531 (2000).

[22] S. Kwan et al.: *Study of Indium and Solder Bumps for the BTeV Pixel Detector.* FERMILAB-CONF-03-363-E (2003).

[23] Hamamatsu Photomultiplier Catalog. `www.hamamatsu.com`

[24] Photomultiplier Tubes, Principles and Applications. Photonis (`www.photonis.com`) (2002).

[25] W. Brückner et al.: *The Electromagnetic Calorimeter in the Hyperon Beam Experiment at CERN.* Nucl. Instrum. Meth. **A313** 345-356 (1992).

[26] R.S. Kessler et al.: *Beam test of a prototype CsI calorimeter,* Nucl. Inst. Meth. **A368** 653-665 (1996).

[27] J.A. Bakken et al." *Results on the Calibration of the L3 BGO Calorimeter with Cosmic Rays.* Nucl. Instrum. Meth. **A343** 456-462 (1994).

[28] GEANT – Detector Description and Simulation Tool, CERN.

[29] W. Brückner et al.: *The Transition Radiation Detector in the Hyperon Beam Experiment WA89 at CERN.* Nucl. Instr. and Meth. **A378** (1996) 451.

[30] N. Terentyev et al.: *E781 Beam Transition Radiation Detector.* SELEX internal Note H-746.

[31] D. Errede et al.: *Use of a Transition Radiation Detector in a Beam of High-Energy Hadrons.* Nucl. Instr. and Meth. **A309** (1991) 386.
D. Errede et al.: *Design and Performance Characteristics of the E769 Beamline Transition Radiation Detector.* IEEE Trans. Nucl. Sci. **36** (1989) 106.

[32] S. Paul: *Particle Identification using Transition Radiation Detectors.* CERN-PPE-91-199.

[33] B. Dolgoshein: *Complementary particle ID: transition radiation and dE/dx relativistic rise.* Nucl. Instr. and Meth. **A433** (1999) 533.

[34] A. Roberts: *A new type of Cherenkov detector for the accurate measurement of particle velocity and direction.* Nucl. Instr. and Meth. **9** (1960) 55.

[35] J. Séguinot and T. Ypsilantis: *Photo-ionization and Cherenkov Ring Imaging.* Nucl. Instr. and Meth. **142** (1977) 377.

[36] E. Nappi, T. Ypsilantis (Eds.): *Proceedings of the First Workshop on Ring Imaging Cherenkov Detectors.* Nucl. Instr. and Meth. **A343** (1994).

[37] T. Ekelöf (Ed.): *Proceedings of the Second International Workshop on Ring Imaging Cherenkov Detectors.* Nucl. Instr. and Meth. **A371** (1996).

[38] A. Breskin, R. Chechik, T. Ypsilantis (Eds.): *Proceedings of the Third International Workshop on Ring Imaging Cherenkov Detectors.* Nucl. Instr. and Meth. **A433** (1999).

[39] *Proceedings of the IV. International Workshop on Ring Imaging Cherenkov Detectors.* Nucl. Instr. and Meth. **A502** (2003).

[40] `http://www.ifisica.uaslp.mx/rich2004`

[41] A. Bideau-Méhu et al.: *Measurement of refractive indices of neon, argon, krypton, and xenon in the $253.7 - 140.4$nm wavelength range.* J. Quant. Spectrosc. Radiat. Transfer **25** (1981) 395.

[42] H.-W. Siebert et al.: *The Omega-RICH.* Nucl. Instr. and Meth. **A343** (1994), 60.

[43] J. Engelfried et al.: *A high-statistics experiment on the U(3100) and on charmed-strange baryons.* Letter of Intent CERN/SPSC/87-8, SPSC/I165 (1987).

[44] A. Forino et al.: *Proposal for a new hyperon beam experiment at the CERN SPS using the Omega facility.* CERN/SPSC/87-43, SPSC/P233 (1987).

[45] J. Engelfried: Ph.D. Thesis, Heidelberg University (1992), unpublished.

[46] W. Beusch et al.: *The RICH counter in the CERN hyperon beam experiment.* Nucl. Instr. and Meth. **A323** (1992) 373.
U. Müller et al.: *The recent performance of the Omega RICH detector in experiment WA89 at CERN.* Nucl. Instr. and Meth. **A371** (1996) 27.
U. Müller et al.: *The Omega RICH in the CERN hyperon beam experiment.* Nucl. Instr. and Meth. **A433** (1999) 71.

[47] R.A. Holroyd et al.: *Measurement of the absorption length and absolute quantum efficiency of TMAE and TEA from threshold to* $120\,nm$. Nucl. Instr. and Meth. **A261** (1987) 440.

[48] J. Russ et al.: *A proposal to construct SELEX.* Fermilab P781 (1987), unpublished.
J. Russ: *Fermilab Hyperon Program: Present and Future Plans.* Nucl. Phys. **A585** (1995) 39c.

[49] M.P. Maia et al.: *A Phototube RICH Detector.* Nucl. Instr. and Meth. **A326** (1993) 496.

[50] V.A. Dorofeev et al.: *The Search for heavy Pentaquark Exotic Baryons with hidden Strangeness in the* $p + n \to (p\Phi) + n$ *and* $p + n \to (\Lambda(1520)\, K^+) + n$ *Reactions at* $E(p) = 70\,GeV$. Physics of Atomic Nuclei **57** (1994) 227.
A. Kozhevnikov et al.: *SPHINX Phototube RICH Detector for Diffractive Production Experiments at Serpukhov Accelerator.* Nucl. Instr. and Meth. **A433** (1999) 164.

[51] R. Richardson and R. Schmitt: Adv. in Cryo. Eng. **41B** (1996) 1907.

[52] L. Stutte, J. Engelfried and J. Kilmer: *A Method to evaluate Mirrors for Cherenkov Counters.* Nucl. Instr. and Meth. **A369** (1996) 69.

[53] U. Müller et al.: *Particle identification with the RICH detector in experiment WA89 at CERN.* Nucl. Instr. and Meth. **A343** (1994) 279.

[54] I. Adam et al.: *Operation of the Cherenkov Detector DIRC of BABAR at High Luminosity.* SLAC–Pub–8783 (2001).

[55] J. Schwiening: *The DIRC Detector at the SLAC B-Factory PEP-II: Operational Experience and Performance for Physics Application* Nucl. Instr. and Meth. **A502** (2003) 67. Preprint SLAC-PUB-7473.

[56] CKM Collaboration, R. Coleman et al.: *CKM – Charged Kaons at the Main Injector – A proposal for a Precision Measurement of the Decay* $K^+ \to \pi^+\nu\bar{\nu}$ *and Other Rare* K^+ *Processes at Fermilab Using the Main Injector.* FERMILAB-P-0905 (1998), unpublished.
CKM Collaboration, J. Frank et al., *CKM - Charged Kaons at the Main Injector - A proposal for a Precision Measurement of the Decay* $K^+ \to \pi^+\nu\bar{\nu}$ *and Other Rare* K^+ *Processes at Fermilab Using the Main Injector.* Proposal (2nd edition) FERMILAB-P-0921, April 2001.

[57] J. Engelfried et al.: *Two RICH Detectors as Velocity Spectrometers in the CKM Experiment.* Nucl. Instr. and Methods **A502** (2003) 62-65. hep-ex/0209020.